Vacuum 217 (2023) 112504

Contents lists available at ScienceDirect

Vacuum

journal homepage: www.elsevier.com/locate/vacuum

Assessment of MHD-relevant parameters in high enthalpy air plasma for flow manipulation experiments

Johannes W. Oswald [a,*], Alexander Behnke [a], Georg Herdrich [a], Sonja I. Schlachter [b], Matthieu Dalban-Canassy [c], Andrea Lani [d]

[a] Institute of Space Systems (IRS), University of Stuttgart, Pfaffenwaldring 29, Stuttgart, 70569, Germany
[b] Karlsruhe Institute of Technology (KIT), Hermann-von-Helmholtz-Platz 1, Eggenstein-Leopoldshafen, 76344, Germany
[c] Absolut System, 2 rue des Murailles, Seyssinet-Pariset, 38170, France
[d] Katholieke Universiteit Leuven, Celestijnenlaan 200b, Leuven, 3001, Belgium

ARTICLE INFO

Keywords:
MHD
High enthalpy air plasma
Optical emission spectroscopy
Stuart number
Magnetic Reynolds number
MEESST

ABSTRACT

As part of the EU New Horizon 2020 project on a Magnetohydrodynamic (MHD) Enhanced Entry System for Space Transportation (MEESST) superconducting magnetic coils will be exposed within an MHD probe to a high enthalpy air plasma. This study assesses key parameters for MHD flow manipulation experiments with the aid of emission spectroscopy measurements of high enthalpy air plasma flows. Thus, the electric conductivity of the plasma and the respective experimental Stuart number and magnetic Reynolds number are derived and compared to literature. The results show that the Lorentz forces are dominating the viscous and inertia forces of the plasma flow by orders of magnitude. When the MHD probe will be exposed to the investigated plasma flow, a significant MHD effect should be observable.

1. Introduction

Flow parameters like the commonly known Prandtl or Reynolds number of aerodynamic problems offer an excellent way to describe and predict common flow behaviors and to outline specific flow regimes. The same is true for the flow parameters and key numbers describing magnetohydrodynamic (MHD) flows, which puts them in a superior position to provide guidance in assessing e.g. the MHD potential of new technologies designed to operate within ionized flows. This is the case since a plasma flow containing charged particles shows a "collective behavior" to a certain extend implicating that the state of the plasma in remote regions remains an impact on global motions and not only on their local conditions [1].

This circumstance is used to the advantage of the MHD flow manipulation experiments within the EU New Horizon 2020 project titled MHD Enhanced Entry System for Space Transportation (MEESST) [2]. One part of the MEESST project the present study contributes to is the investigation to which extend a high enthalpy air plasma flow can be manipulated to mitigate the stagnation heat flux measured by a dedicated plasma wind tunnel probe. For this purpose, a plasma probe, which will be titled "MHD probe" in the following, was explicitly designed within the MEESST project by Absolut System accommodating a high temperature superconducting (HTS) magnet developed by the Karlsruhe Institute of Technology [3] (see Fig. 1).

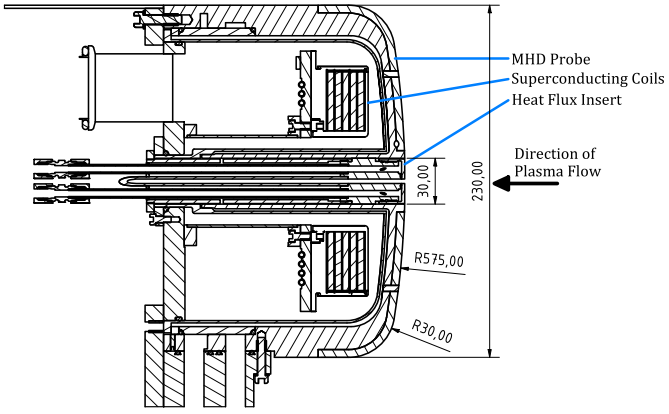

Fig. 1. Cross-section view of the MHD probe. On the center axis, the calorimetric measurement insert for the simultaneous stagnation heat flux and pressure measurements is sketched and the relevant dimensions of the nose are provided [2].

Early theoretical concepts on the heat flux control during an atmospheric re-entry by means of magneto-aerodynamics are dated back to

* Corresponding author.
E-mail address: oswaldj@irs.uni-stuttgart.de (J.W. Oswald).

https://doi.org/10.1016/j.vacuum.2023.112504
Received 3 March 2023; Received in revised form 1 August 2023; Accepted 13 August 2023
Available online 24 August 2023

the 1960's [4,5]. Resler and Sears [4] also investigated the electric conductivity of air plasma and seeded air plasma depending on the Mach number. They found that the seeded elements are dominating the electric conductivity and are increasing the conductivity by orders of magnitude even in weakly ionized air flows compared to the pure air plasma. This let them conclude that electro-magnetic effects may especially be significant for e.g. controlling the heat transfer and skin friction in boundary layers of re-entering missiles when the conductivity of air is artificially increased by seeding. Furthermore, Jarvinen [6] found in his theoretical studies that by using MHD shielding during high speed re-entry, the thermal protection system mass can be significantly reduced despite the additional weight of the coils.

To date, multiple studies were performed on the MHD based heat flux mitigation for reentry purposes both experimentally and numerically. A qualitative review is provided by Giacomelli et al. [7]. The interested reader should refer especially to the work by Knapp et al. [8],Kranc et al. [9],Takizawa et al. [10], and Kawamura et al. [11], who used argon gas plasma flows in continuous plasma wind tunnel (PWT) facilities and to recent studies by Lefevre et al. [12] who used air as the working gas in their shock tube facility to simulate the properties of superorbital earth reentries.

The MEESST project combines the advantage of a continuous PWT facility [13] with the enhancement of a superconducting magnet and air as the working gas. Consequently, the determination of the MHD flow parameters are a key element to be able to compare results obtained in the different test facilities and conditions. In this study, the MHD flow parameters like the magnetic Reynolds number and the Stuart number are determined to estimate the interaction potential of a magnetic field with the high enthalpy air plasma flow, which experimental proof has been shown in the same PWT facility by Knapp et al. [8] using a high enthalpy argon plasma flow. The magnetic field strength is chosen to be similar to the one of the MHD probe, which will be exposed to the plasma flow in future tests.

2. MHD flow parameters

In principle, two MHD flow parameters, the magnetic Reynolds number and the Stuart number or interaction parameter, are essential to estimate the MHD potential of a conducting fluid [14]. The in literature on MHD often mentioned Hartmann number has a significant importance in metallurgy processes but the underlying boundary layer effects are not restricted to such applications. Since the boundary layer is suspected to play an important role in the heat transfer control [4], it is also considered in this study. Ultimately each of these parameters is relying on the knowledge of the flow's electric conductivity. This is why its determination is outlined first, followed by the Hall parameter and the MHD flow parameters.

2.1. Electric conductivity

The electrical conductivity σ_0 in a partially ionized air plasma shown by Brunner [15] is carried by the electrons and restrained by electron–ion and electron–neutral collisions

$$\sigma_0 = \frac{n_e e^2 \bar{\tau}_e}{m_e} = \frac{n_e e^2}{m_e \sum \nu_{ej}} \quad , \quad j \in \{i, n\} \ , \tag{1}$$

with the electron number density n_e, the electron charge e, the electron mass m_e, and the average time between collisions of an electron $\bar{\tau}_e$. The collision frequency is

$$\nu_{ej} = {\tau_{ej}}^{-1} = n_j \sigma_{ej} \upsilon_{e,thermal} = n_j \sigma_{ej} \sqrt{\frac{8 k_B T_e}{\pi m_e}} \ , \tag{2}$$

with the particle density n_j, the collision cross section of an e-j collision σ_{ej}, the thermal velocity of the electrons $\upsilon_{e,thermal}$, the Boltzmann constant k_B, and the electron temperature T_e. The mean free time for electron–ion collisions τ_{ei} is dominated by Coulomb collisions shown by Dinklage et al. [16] as

$$\tau_{ei} = \frac{16 \pi \epsilon_0^2 \sqrt{m_e} \left(k_B T_e\right)^{3/2}}{\sqrt{3} n_e e^4 \ln \Lambda_C} \ , \tag{3}$$

with the vacuum permittivity ϵ_0 and the Coulomb logarithm $\ln \Lambda_C$. The collision cross sections of electron–neutral (index en) collisions are larger than the gas kinetic cross sections due to polarization of the neutral particles by the electrons [17]. Brunner [15] assumes for high temperature air $\sigma_{en} = 1 \times 10^{-19}\,\mathrm{m}^2$ based on [18], Itikawa [19] shows cross sections for electron–atomic oxygen and electron–atomic nitrogen in the order of $\sigma_{en} = 1 \times 10^{-19}\,\mathrm{m}^2$ *to* $1 \times 10^{-20}\,\mathrm{m}^2$. With the experimental conditions of $T_e \leq 1.2\,\mathrm{eV}$, $n_e \leq 1 \times 10^{21}\,\mathrm{m}^3$ and a degree of ionization $\geq 10\,\%$ the fraction of the electron–neutral collision frequency is $\nu_{en}/\nu_e \leq 3\,\%$ and, therefore, the electron–neutral collisions could be neglected.

2.2. Hall parameter

In a magnetic field, charged particles are deflected perpendicularly to their velocity vector and the magnetic field and gyrate around the field lines. Cross field transportation is bound to collisions where the gyration center is moved. The Hall parameter

$$\beta = \omega_e \bar{\tau}_e = \frac{eB}{m_e \sum \nu_{ej}} \quad , \quad j \in \{i, n\} \ , \tag{4}$$

with the magnetic field strength B, is a measure of this restriction of the cross field transportation of charged particles. The electrical conductivity perpendicular to the magnetic field is

$$\sigma_\perp = \sigma_0 \left(\frac{1}{1 + \left(\omega_e \bar{\tau}_e\right)^2} \right) \ . \tag{5}$$

2.3. Magnetic Reynolds number

One of the major parameters relevant for MHD problems is the ratio of advection to diffusion of a magnetic field described by the magnetic Reynolds number

$$\mathrm{R_m} = \mu_0 \sigma_0 u L \ , \tag{6}$$

where $\mu_0 = 4\pi 10^{-7}\,\mathrm{N\,A^{-2}}$ is the permeability of free space, L is a characteristic length scale, and u is the flow velocity. In general, two cases are to be considered:

1. When $\mathrm{R_m} > 1$ as in highly conducting fluids, the diffusion is weak and the magnetic field lines are more or less frozen into the conducting medium and behave like elastic bands.
2. When $\mathrm{R_m} \ll 1$, imposed fields are dominant compared to the induced fields and they become negligible because the magnetic field is barely influenced by the plasma flow velocity and topology [14].

In Case 1, the flow velocity has a great influence on the magnetic field configuration and Alfvén waves are resulting from near-elastic oscillations caused by small disturbances of the medium. The required restoring force for the vibration is provided by the magnetic field and the frequency of the Alfvén waves are of the order of $\omega \sim \upsilon_a / L$, with υ_a been the Alfvén velocity defined as

$$\upsilon_a = \frac{B}{\sqrt{\rho \mu}} \ , \tag{7}$$

where ρ denotes the density of the conducting medium. Another consequence of Case 1 is that during the motion of the conducting fluid the magnetic flux tends to be conserved while passing through any closed loop, which is composed of the same material particles.

In Case 2, the magnetic damping time $\tau_m = \left[\sigma_0 B^2 / \rho\right]^{-1}$ becomes the relevant time scale since the mechanical motions are damped by converting the kinetic energy into heat. This is done by Joule dissipation.

Thus, τ_m rather than v_a is at low R_m the characteristic over which the Lorentz force is influencing the flow. In this case, the flow velocity can be altered by the magnetic field by exciting/suppressing bulk motions, or altering the structure of the boundary layer [14].

Batchelor et al. [20] states a third regime where $R_m = \mathcal{O}(1)$. In this regime, dynamo instabilities may occur due to arising turbulence from dynamical instabilities. However, those instabilities are requiring a dominating induction over diffusion.

2.4. Hartmann number

The Hartmann number is defined as

$$\mathrm{Ha} = BL\sqrt{\frac{\sigma_0}{\rho\nu}}\,, \tag{8}$$

where ν is the kinematic viscosity of the fluid, and the square of the Hartmann number describes the ratio of Lorentz to viscous forces in case of $R_m \ll 1$. Discussions of the Hartmann number are often occurring in the context of duct flows of liquid metals at low R_m due to the arising Hartmann boundary layer (Hartmann layers). Nevertheless, this is a general MHD boundary layer effect, where the orientation of a static magnetic field plays a vital role in the complete transformation of the boundary layer's nature, e.g. changing its characteristic thickness d to the Hartmann layer thickness $\delta = d/\mathrm{Ha}$ normal to the magnetic field [14].

Since the MHD probe will also employ a steady magnetic field, this effect might be of significance for the flow manipulation experiments in high enthalpy air plasma where the thickening of the shock standoff distance is one of the expected outcomes according to literature [7–9, 12].

2.5. Stuart number

The Stuart number St, which is also known as interaction parameter N [14], provides at low magnetic Reynolds numbers a ratio of Lorentz to inertia forces,

$$\mathrm{St} = \frac{\sigma_0 B^2 L}{\rho u} = \frac{L}{u\tau_m}\,, \tag{9}$$

where $\tau_m = \left[\sigma_0 B^2/\rho\right]^{-1}$ is the magnetic damping time. Macheret et al. [21] includes an additional product of the Hall parameter $\Omega_e\Omega_i$ as ion-slip correction term

$$\mathrm{St} = \frac{\sigma_0 B^2 L}{\left(1+\Omega_e\Omega_i\right)\rho u}\,, \tag{10}$$

with the electron Hall parameter $\Omega_e = eB/\left(m_e\nu_{en}n\right)$ and the ion Hall parameter $\Omega_i = eB/\left(m_n\nu_{in}n\right)$. The size n refers to the total particle density, m_n to the mass of the species, ν_{in} to the ion–neutral collision frequency, and ν_{en} to the electron–neutral collision frequency. In this study, the ion-slip can be neglected due to the ground state particle density been of $n = \mathcal{O}(1\times10^{21}\,\mathrm{m}^{-3})$ leading to an ion slip correction term of $\Omega_e\Omega_i = \mathcal{O}(1\times10^{-38})$ at an ionization degree of $> 10\,\%$ and thus, the Stuart number increases proportional to B^2.

In case of experiments in PWT it may makes sense in some cases to define an experimental Stuart number St_{ex}, which considers mass conservation [8]. Thus, the experimental Stuart number becomes

$$\mathrm{St}_{ex} = \frac{\sigma_0 B^2 L}{\rho u} = \frac{\sigma_0 B^2 LA}{\dot{m}}\,, \tag{11}$$

where $\dot{m}$ is the mass flow rate and A denotes the cross section of the plasma plume.

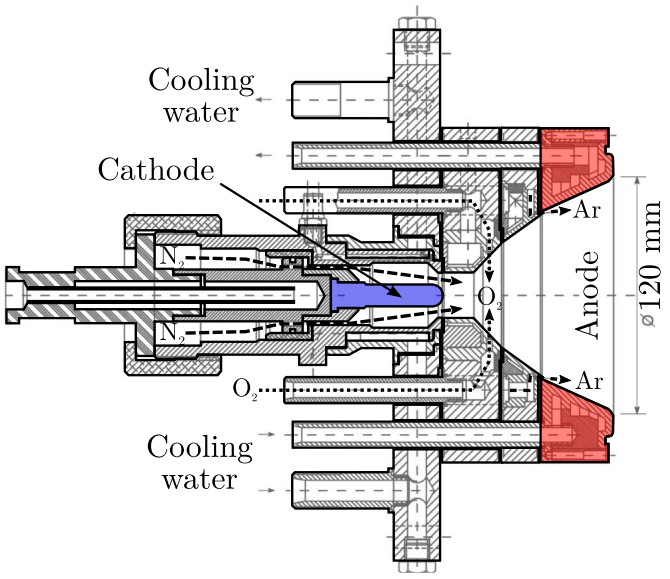

Fig. 2. Cross-section view of the SF-MPG RD5 installed inside the PWK1 facility to generate high enthalpy air plasma flows.

3. Experimental procedure

At IRS multiple plasma wind tunnel (PWT, German naming convention of the facilities itself is PWK) facilities are available, which are equipped with a variety of plasma generator types to generate plasma flows at different pressure, Mach number, heat flux, and mass specific enthalpy levels [13]. Thus, a wide range of the thermo-chemical flow environments of typical planetary re-entry trajectories can be simulated. In the following, the experimental facility PWK1 and the employed diagnostics by means of optical emission spectroscopy are described.

3.1. Experimental facility

For the purpose of this study, the self-field magnetoplasmadynamic plasma generator (SF-MPG) RD5 inside the facility PWK1 was used to generate the high enthalpy gas flows at comparatively low-pressure conditions targeting the early re-entry phases at high altitudes and high velocities associated with the extreme heat fluxes of typical high-elliptic and hyperbolic entry trajectories. A cross section of RD5 with indications of the working gas injections is visualized in Fig. 2 and a detailed description of RD5 can be found in [22]. PWK1 itself is a 6 m long and 2 m diameter stainless steel vacuum tank connected to an in-house water cooling and vacuum system capable of up to 250 000 $\mathrm{m^3\,h^{-1}}$ in suction power at 10 Pa ambient pressure inside PWK1.

The working gas of RD5 was a mixture of 77.20 vol% nitrogen, 20.45 vol% oxygen, and a trace amount of 2.35 vol% argon. The generator operating conditions, as well as the applied intrusive diagnostic techniques, are thoroughly described in [23]. The operational parameter of RD5 and PWK1 are outlined in Table 1. An overview of the plasma condition at multiple axial distances x to the generator exit plane is provided in Table 2. The axial position $x = 200$ mm and $x = 250$ mm are thereby additions to [23] and may serve as boundary conditions at the inflow of numerical simulations.

3.2. Optical plasma diagnostics

Emission spectroscopy enables the investigation of a wide range of plasma parameters without disturbing the actual plasma flow, which makes it an indispensable tool in non-intrusive plasma diagnostics.

Table 1
Overview on the operating parameters of the SF-MPG RD5 [23].

Parameter	Unit	Value
Current I	A	1305
Voltage U	V	104
Electrical power P	kW	136.1
Total cooling power Q	kW	39.2
Thermal efficiency η_{th}	%	71.2
Gas flow $\dot{m}_{N_2}$	g s^{-1}	6.91
Gas flow $\dot{m}_{O_2}$	g s^{-1}	2.09
Gas flow $\dot{m}_{Ar}$	g s^{-1}	0.30
Bulk enthalpy h_B	MJ kg^{-1}	10.54
Plenum chamber pressure p_{cc}	hPa	151.2
Ambient pressure p_{amb}	Pa	175

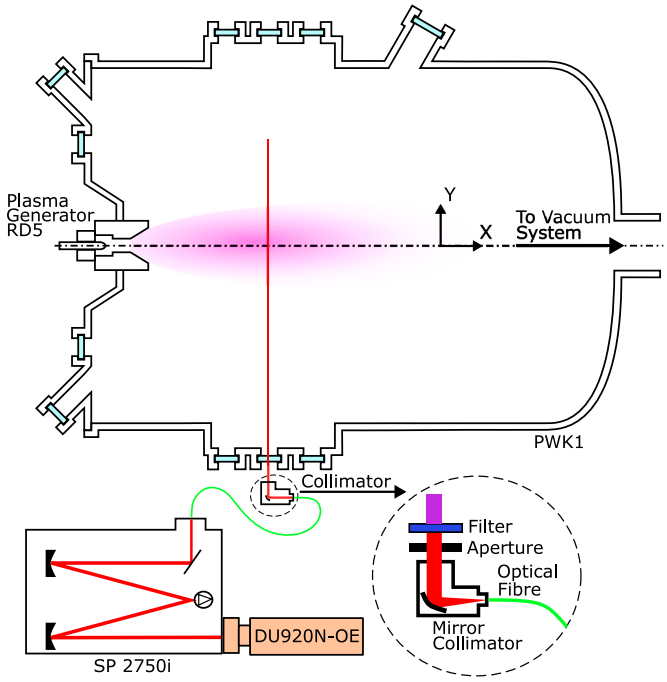

Fig. 3. Sketch of the OES setup installed outside PWK1 to collimate the plasma emissions at different x and radial positions. An Acton SpectraPro SP2750i was used as the spectrometer and the CCD camera Andor Newton DU920N-OE served as the detector while the emissions were collimated with a mirror collimator and guided into the SP2750i via an optical fiber.

As the MHD parameter of interest are ultimately depending on the electron number density n_e and temperature T_e, the following optical emission spectroscopy (OES) approach was employed to determine both parameter.

In Fig. 3 the OES setup is sketched. The emissions of the radiating plasma were collimated with a Thorlabs mirror collimator RC08SMA-F01 placed on a rotation platform. Thus, one vertical sweep through the plasma achieved an angular resolution of 0.5° corresponding to a radial resolution of 10.8 ± 0.9 mm per data point. Although rather coarse, this resolution end up to be sufficient for a Fourier-like Abel inversion as proposed by [25], which was implemented on the basis of [26].

As spectrometer served a Princeton Instruments Acton SpectraPro SP2750i. The spectrometer is a Czerny–Turner type model with a focal length of 750 mm and its CCD detector camera was an Andor Newton DU920N-OE. The detailed OES system specifications are listed in Table 3.

The acquired spectra were absolute calibrated with a Gigahertz-Optik ISS-5P Integrating Sphere Source for Spectral Radiance of which the spectral radiance Φ is known in W nm^{-1} sr^{-1} m^{-2}. By assuming a rotationsymmetric plasma plume, the Abel inversion enables the determination of the spectral emissivity ϵ_{jk} of each spectral line at each data point in W nm^{-1} sr^{-1} m^{-3}. Here, the index k denotes the ground state and j the excited state. The emission coefficient of a spectral line can be defined by:

$$\epsilon_{jk} = \frac{hc_0}{4\pi\lambda_{jk}} A_{jk} n_j \,, \tag{12}$$

with h been the Planck's constant, c_0 the speed of light in vacuum, A_{jk} the transition probability (Einstein coefficient), and λ_{jk} the emitted wavelength.

The Abel inversion requires besides a suitable radial resolution an optically thin plasma. The opacity of the plasma was estimated based on [27]. For an expected electron temperature range of $0.6\,\text{eV} < T_e < 1.3\,\text{eV}$, the optical depth τ of the considered wavelength range been of $\tau < \mathcal{O}(1 \times 10^{-7}) \ll 1$. Thus, the opacity and subsequently radiation transport is negligible and the plasma is optically thin [27].

Considering two energy levels E_j and E_p been in local thermal equilibrium (LTE), the relation between the atomic densities of respective line intensities n_j, n_p are Boltzmann distributed according to:

$$\frac{n_j}{n_p} = \frac{g_j}{g_p} \exp\left[-\frac{E_j - E_p}{k_B T}\right] \,, \tag{13}$$

where g_j, g_p are the statistical weights. Following Eq. (13), and taking the logarithm in both sides provides the population of each energy level:

$$\ln\left(\frac{n_{jk}}{g_{jk}}\right) = \frac{-E_j}{k_B T} + C \,, \tag{14}$$

where C is a constant. This is the well known Boltzmann plot method to determine rather analytically the electronic excitation temperatures [28].

While the method is well known and rather straight forward to conduct, multiple authors have shown the limitations of using the electronic excitation temperature as an estimator for the electron temperature if the observed plasma state departs from a local thermal equilibrium [28,29]. van der Sijde and van der Mullen [29] proposed a methodology for plasma states in close-to-LTE which are satisfying $k_B T_e / E_i \ll 1$. According to previous OES studies [30,31] performed inside PWK1 with RD5 and air been the working gas at fairly comparable operating conditions of the generator, the electron temperature is expected to be within the range of $0.6\,\text{eV} < T_e < 1.3\,\text{eV}$. For nitrogen, this results in $k_B T_e / E_i$ been within 0.04 to 0.09 and for oxygen been within 0.04 to 0.1, fairly satisfying the criterion of [29].

The authors make use of the Boltzmann plot by extrapolating only the high excited states to a fictitious level $\eta_\infty = n_\infty / g_\infty$ at the ionization energy level $E_\infty = E_i$ (see Fig. 4) and including other plasma parameters like the gas temperature T_{gas} and pressure $p_{gas} = n_1 k_B T_{gas}$ for the determination of the ground state $\eta_1 = n_1 / g_1$.

The gas temperature and density of the plasma is estimated with an iterative NASA-Glenn Chemical Equilibrium Program CEA2 [32] (CEA) approximation. The assumptions made in the hp-mode are that the flow is in chemical equilibrium and an adiabatic combustion at constant pressure is present. This means that the system's enthalpy and pressure remains constant while the system's overall chemical composition and temperature are adjusted to minimize the Gibbs free energy [32]. With the first iteration, an initial sonic velocity is derived. Using the determined Mach numbers of the experiments in [23], the flow velocity and the kinetic enthalpy contribution h_{kin} to the measured total mass-specific stagnation enthalpy is calculated according to:

$$h_{kin} = \frac{1}{2} u^2 \,. \tag{15}$$

This contribution is subtracted from the enthalpy used in the second iteration and the process is repeated until the residuum is < 1 % [33].

With the energy levels been those of the ground state and the ionization limit, the electron temperature can be determined from:

$$\frac{E_i}{k_B T_e} = \ln\left[\frac{p_{gas}}{g_1 b_1 \eta_\infty k_B T_{gas}}\right] \,, \tag{16}$$

Table 2
Overview of the center line stagnation point parameters at four axial distances x to the plasma generator exit plane [23].

Parameter	Unit	Position 1	Position 2	Position 3	Position 4
Axial position x	mm	200	250	300	355
Reference heat flux $\dot{q}_{\mathrm{CuO,cw}}$ [a]	kW m^{-2}	3376.8 ± 54.1	2321.0 ± 47.3	1594.8 ± 28.1	1143.9 ± 25.5
Scaled heat flux $\dot{q}_{\mathrm{CuO,cw}}$ [b]	kW m^{-2}	2061	1416	973	698
Stagnation pressure p_0	Pa	675 ± 1.9	591 ± 1.5	523 ± 1.3	408 ± 1.2
Mach number Ma	–	$1.72^{+0.01}_{-0.28}$	$1.59^{+0.01}_{-0.27}$	$1.50^{+0.01}_{-0.30}$	$1.40^{+0.01}_{-0.28}$
Mass-specific stagnation enthalpy h	MJ kg^{-1}	$140.6^{+7.8}_{-8.1}$	$103.9^{+5.8}_{-6.2}$	$76.4^{+4.2}_{-4.8}$	$57.6^{+3.2}_{-3.7}$
Equilibrium ionization degree α_{tot} [c]	%	41.2	30.0	20.4	10.1

[a] CuO, cold wall, flat faced Ø 80 mm cylinder (measured [23]).
[b] CuO, cold wall, flat head Ø 230 mm MHD probe (calculated using effective radius scaling of [24]).
[c] Iterative CEA approximation within the hp-mode with exclusion of the kinetic contribution to the mass-specific stagnation enthalpy.

Table 3
SP2750i and DU920N-OE CCD system specifications.

System component	Parameter value
focal length	750 mm
slit width	10 µm
aperture ratio	f/9.7
focal plane size	14x25 mm^2
DU920N-OE CCD image area	6.6x26.6 mm^2
DU920N-OE CCD pixel size	26x26 µm^2
DU920N-OE CCD sensor resolution	255x1024 pixel^2
DU920N-OE CCD usable resolution	255x962 pixel^2
DU920N-OE CCD linearity (maximum)	1%
DU920N-OE CCD imaging mode	Full vertical binning
grating 1 groove density	300 mm^{-1}
grating 1 blaze wavelength	500 nm
grating 1 dispersion	0.114 nm pixel^{-1}
grating 1 optical resolution	0.227 nm
grating 1 wavelength coverage on CCD	109.283 nm
grating 2 groove density	600 mm^{-1}
grating 2 blaze wavelength	200 nm
grating 2 dispersion	0.056 nm pixel^{-1}
grating 2 optical resolution	0.112 nm
grating 2 wavelength coverage on CCD	54.064 nm

with b_1 been the ratio of the ground-state density n_1 to the Saha-density n_{1s}. For LTE, $b_1 \equiv 1$, while van der Sijde and van der Mullen [29] define the boundary of Close-to-LTE as:

$$0.1 \leq b_1 \equiv \frac{n_1}{n_{1s}} \leq 10\ , \tag{17}$$

with $b < 1$ referring to recombining plasmas and $b > 1$ referring to ionizing plasmas.

In a similar manner to Eq. (16), the electron number density n_e can be estimated. The Saha-equation defined as:

$$\frac{n_{j+1} n_e}{n_j} = \frac{g_{j+1}}{Q_j} \frac{\Lambda^3}{2} \exp\left[-\frac{E_{i,j}}{k_B T_e}\right]\ , \tag{18}$$

with

$$\Lambda = \sqrt{\frac{h^2}{2\pi m_e k_B T_e}}\ , \tag{19}$$

where Λ is the thermal wavelength of the electrons, and $E_{i,j}$ is the ionization energy of the ionization level j, can be rewritten in the form by van der Sijde and van der Mullen [29]:

$$\frac{n_{k,i}}{g_{k,i}} = n_e \frac{n_i}{Q_i} \frac{\Lambda^3}{2}\ , \tag{20}$$

where the particle density of the level k of the ionized state i corresponds to η_∞ and Q_i is the partition sum of all ionized particles with density n_i. With the assumption of quasi-neutrality, and by neglecting $N_2^+ = \mathcal{O}(1 \times 10^{17}\ \mathrm{m}^{-3})$, the electron number density is composed of singly ionized nitrogen $n_{i,N}$ and oxygen $n_{i,O}$:

$$n_e = n_{i,N} + n_{i,O}\ . \tag{21}$$

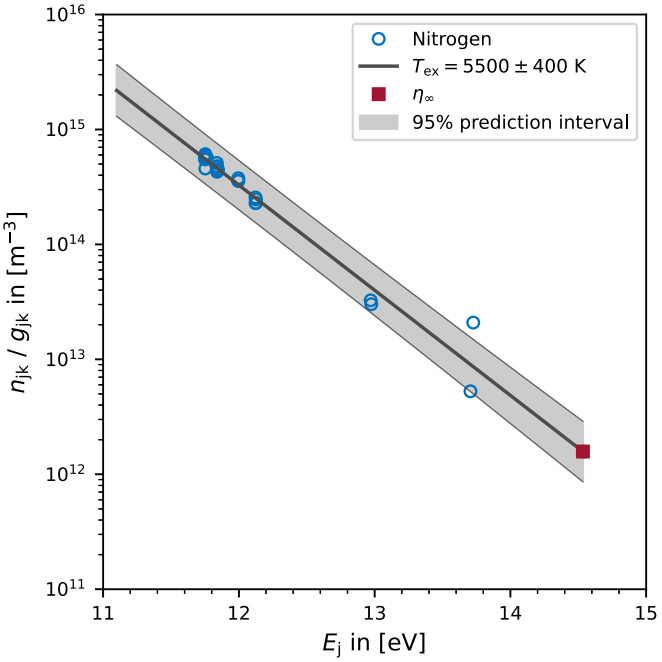

Fig. 4. Typical Boltzmann plot of Abel inverted levels of nitrogen on the plasma center line of position 3 in Table 2, which are used for the determination of $\eta_\infty = n_\infty / g_\infty$ by extrapolation to a fictitious level $E_\infty = E_i$ [29]. The displayed envelope of the prediction interval is calculated according to [34].

It follows from Eqs. (20) and (21):

$$n_e = \sqrt{\frac{2}{\Lambda^3}\left(\frac{n_{i,N}}{g_{i,N}} Q_{i,N} + \frac{n_{i,O}}{n_{i,O}} Q_{i,O}\right)}\ , \tag{22}$$

with $n_{i,N}/g_{i,N} = \eta_{\infty,N}$ and $n_{i,O}/g_{i,O} = \eta_{\infty,O}$. The partition sums of ionized nitrogen $Q_{i,N}$ and oxygen $Q_{i,N}$ are linear interpolated from [35].

In Eq. (21) the contribution of Ar^+ was neglected due to the trace amount of argon gas introduced tangentially to the flow at the copper anode of the RD5 SF-MPG (see Fig. 2). The argon gas is used primarily as a supportive ion source compensating a potential lack of charged particles in the anode fall region, which prevents the onset of instabilities and enlarges the operational envelope of RD5 [22].

4. Results and discussion

In the following the results of the OES are presented, which enabled along with CEA calculations the determination of the aforementioned MHD flow parameters, namely the magnetic Reynolds number, Stuart number, and Hartmann number. Each spectrum was acquired in free stream conditions using OES as sketched in Fig. 3. Despite the fact,

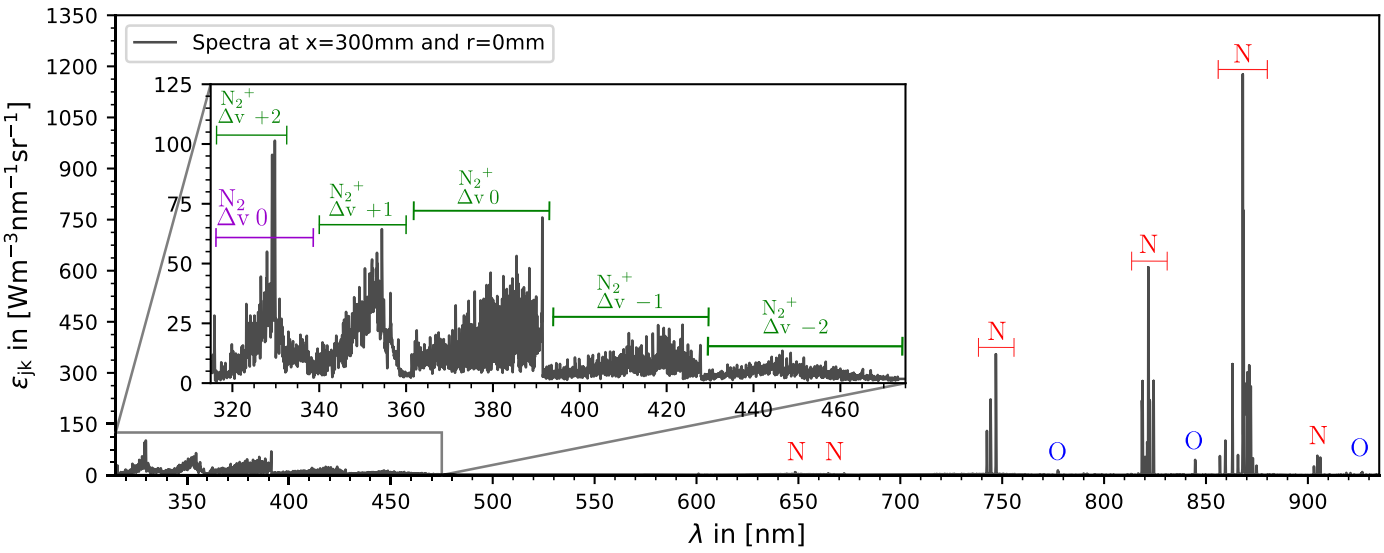

Fig. 5. Absolute calibrated and Abel inverted emission spectrum at position 3 on the plasma center line. Identified emissions of the radiating air plasma species are marked in the spectrum.

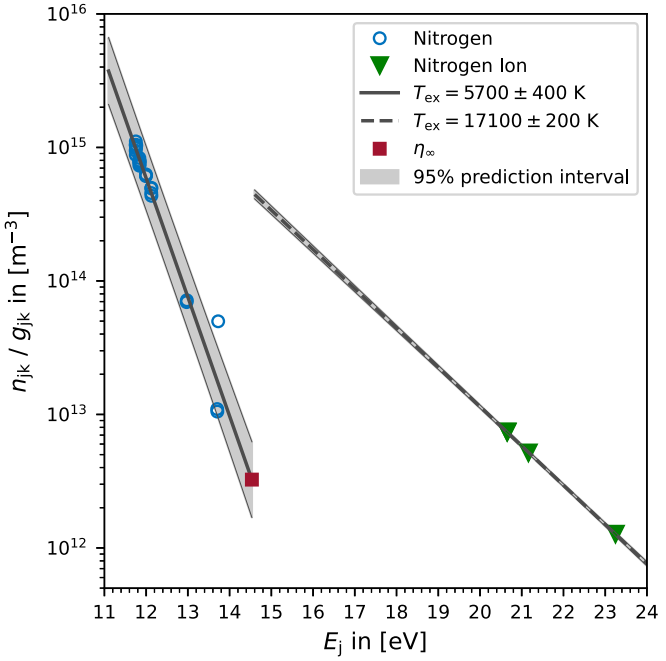

Fig. 6. Typical Boltzmann plot of Abel inverted levels of nitrogen and ionized nitrogen on the plasma center line of position 1 in Table 2. The displayed envelope of the prediction interval is calculated according to [34]. The excitation temperatures of both species differ by 1×10^4 K indicating that both are not in LTE, although the quality of the linear regression indicates that each species follows a Boltzmann distribution.

that the MHD probe displayed in Fig. 1 will alter the flow significantly, the calculated MHD flow parameter provide indications of the general MHD potential of the investigated plasma flow. Thus, an expectation baseline is set for the follow-up MHD flow manipulation experiments, which will be conducted in the presented plasma conditions.

Experienced scientist with a large background in plasma diagnostics, chemistry, plasma wind tunnels and especially spectroscopy.

Fig. 5 exemplary displays a spectrum of the plasma free stream at position 3 (see Table 2) with indications of the identified species. Only at position 1, four faint singly ionized nitrogen N^+ lines could be identified within a radius of $r \leq 30$ mm around the plasma center line. The respective Boltzmann plot of significantly radiating levels of N and N^+ at the center line of position 1 is shown in Fig. 6. The excitation temperature of N is thereby $T_{ex,N} = 5.7 \times 10^3 \pm 0.4 \times 10^3$ K, while the excitation temperature of N^+ is $T_{ex,N^+} = 17.1 \times 10^3 \pm 0.2 \times 10^3$ K. This clearly indicates that the plasma plume is at position 1 not yet equilibrated on the center line and the excitation temperature would not be an appropriate estimator of the electron temperature. It is suspected that the observed discrepancy in the excitation temperature of N^+ and N is mainly motivated by the discharge of RD5 and not by, e.g. radiative transport in the plasma plume.

The outlined approach to determine the electron temperature and density in PLTE and Close-to-LTE plasmas as proposed by van der Sijde and van der Mullen [29] attempts to mitigate this by limiting the error sources of the linear regression fit in the Boltzmann plot method and by involving an estimation of the ground state with the ideal gas law. Nevertheless, the determined electron temperature and density can only be understood as an indicator of the variables' magnitudes. In an attempt to define meaningful uncertainties of the electron temperature and density, the uncertainties of the extrapolated and fictitious level $\eta_{\infty,N}$ were estimated with the envelopes of 95 % prediction intervals, which were derived according to [34].

As can be seen from Table 4, calculations made with the aid of CEA seem to fit to some extend within the estimated uncertainties of the experimentally determined electron densities, although CEA assumes that the species are in chemical equilibrium. The highest agreement occurs at position 3 where the enthalpy of the flow corresponds to a hyperbolic re-entry. This led to the conclusion, that certain flow parameters, like the kinematic viscosity, might be reasonably predicted inside the correct order of magnitude and thus the respective MHD flow parameters.

The MHD flow parameter itself are indicating the following consequences for the flow manipulation experiments and their numerical rebuild within the MEESST project.

The magnetic Reynolds number is $R_m = \mathcal{O}(1 \times 10^{-1})$. While this is comparable to other plasma conditions reported at IRS even with argon as working gas [8], the ones achieved in shock tube facilities by Lefevre et al. [12] are $R_m > 1$. Depending on the literature, a $R_m = \mathcal{O}(1 \times 10^{-1})$ is reasonably low for assuming that the induced magnetic fields in the plasma flow are negligible. This would enable the decoupling of the electromagnetic and flow field [36]. However, dynamic instabilities are likely to occur at $R_m = \mathcal{O}(1)$ [20] and, therefore, the decoupling assumption should at least be verified by theoretical considerations of a weakly coupled electromagnetic and flow field.

Table 4
Results of the OES and MHD flow parameter determination at the investigated positions 1–4.

Parameter	Unit	Position 1	Position 2	Position 3	Position 4
Excitation temperature $T_{ex,N}$	1×10^3 K	5.7 ± 0.4	5.4 ± 0.3	5.5 ± 0.4	5.3 ± 0.4
Electron temperature T_e	1×10^3 K	$9.2^{+0.5}_{-0.3}$	$8.8^{+0.4}_{-0.2}$	$8.8^{+0.4}_{-0.2}$	$8.8^{+0.5}_{-0.3}$
Equilibrium temperature T_{CEA} [a]	1×10^3 K	10.6	9.8	9.2	8.5
Electron number density n_e	1×10^{20} m^{-3}	$4.0^{+1.8}_{-1.0}$	$2.7^{+1.1}_{-0.6}$	$2.8^{+1.1}_{-0.6}$	$3.0^{+1.4}_{-0.7}$
Equilibrium electron number density $n_{e,CEA}$ [a]	1×10^{20} m^{-3}	4.9	3.9	2.8	1.5
Ionization degree α	1×10^{-1}	$3.4^{+1.7}_{-1.1}$	$2.1^{+1.0}_{-0.6}$	$2.1^{+0.9}_{-0.6}$	$2.0^{+1.0}_{-0.6}$
Equilibrium ionization degree α_{CEA} [a]	1×10^{-1}	4.1	3.0	2.0	1.0
Electrical conductivity σ_0	1×10^2 S m^{-1}	$7.7^{+5.0}_{-2.6}$	$7.1^{+4.2}_{-2.3}$	$7.0^{+3.7}_{-2.0}$	$7.1^{+4.7}_{-2.4}$
Hall parameter β	1×10^1	$1.0^{+0.4}_{-0.2}$	$1.3^{+0.5}_{-0.3}$	$1.2^{+0.5}_{-0.3}$	$1.2^{+0.6}_{-0.3}$
Reduced Hall parameter β_{red}	1×10^1 T^{-1}	$1.2^{+0.6}_{-0.3}$	$1.6^{+0.7}_{-0.4}$	$1.6^{+0.6}_{-0.3}$	$1.5^{+0.7}_{-0.4}$
Magnetic Reynolds number R_m [b]	1×10^{-1}	$1.7^{+1.1}_{-0.6}$	$1.3^{+0.6}_{-0.4}$	$1.1^{+0.6}_{-0.3}$	$0.9^{+0.6}_{-0.3}$
Stuart number St [b]	1×10^2	$1.5^{+1.0}_{-0.5}$	$1.3^{+0.8}_{-0.4}$	$1.3^{+0.7}_{-0.4}$	$1.2^{+0.8}_{-0.4}$
Hartmann number Ha [c]	1×10^1	$8.0^{+3.0}_{-1.0}$	$6.0^{+2.0}_{-1.0}$	$5.0^{+1.0}_{-1.0}$	$5.0^{+2.0}_{-1.0}$
Squared Hartmann number Ha^2 [c]	1×10^3	$6.6^{+4.3}_{-2.2}$	$3.3^{+2.0}_{-1.1}$	$2.5^{+1.3}_{-0.7}$	$2.1^{+1.4}_{-0.7}$
Reynolds number Re_{CEA} [a,b]	1×10^1	4.4	2.5	2.0	1.7

[a] Iterative CEA approximation within the hp-mode with exclusion of the kinetic contribution to the mass-specific stagnation enthalpy.
[b] Characteristic length $L = 30$ mm equal to the diameter of the heat flux insert of the MHD probe.
[c] Characteristic length $L = 30$ mm equal to the diameter of the heat flux insert of the MHD probe. Magnetic field strength equal to $B = 0.8$ T, corresponding to the expected field strength of the superconducting magnet operated with 50 A at the probe tip.

As the Stuart number is $St = \mathcal{O}(1 \times 10^2)$, the Lorentz force density is by two orders of magnitudes greater than the inertia forces, respectively the plasma total pressure [36]. Thus, the magnetic forces should have a significant influence on the plasma flow throughout flow manipulation experiments. The experimental Stuart number $St_{ex} \approx 70$ is comparable to those of the shock tube experiments with air by Ziemer and Bush [37] ($St_{ex} \approx 160$) and mostly exceeds those of PWT experiments with argon ($St_{ex} \approx 1$ [9], $St_{ex} \approx 31$ [8]). Since the squared Hartmann number is $Ha^2 = \mathcal{O}(1 \times 10^3)$ and the magnetic Reynolds number can be considered as low, the viscous forces are dominated by the Lorentz forces by orders of magnitude [14]. The squared Hartmann number can in this case also be derived as $Ha^2 = StRe$ and thus, the Reynolds number Re is also provided in Table 4.

With the Hall parameter been $beta = \mathcal{O}(1 \times 10^1)$, Hall effects, such as the ion slip or the reduction of the electrical conductivity perpendicular to the magnetic field, must be considered in numerical simulations. The electrical conductivity perpendicular to the magnetic field is about 1 % of the electrical conductivity $\sigma_\perp \approx 0.01\sigma_0$. Therefore, a Hall current should be present when the MHD probe is introduced to the plasma flow, reducing the effective conductivity of the plasma [15].

Another consequence of the Hall parameter been $\beta = \mathcal{O}(1 \times 10^1)$ is related to the surface conductivity of the MHD probe wall. Simulations on the influence of the Hall effect on the MHD shielding by Otsu et al. [38] indicate that the heat flux in the stagnation point of a conducting wall is increased at $\beta_{red} = \mathcal{O}(1 \times 10^1\ T^{-1})$, while been reduced as expected in the insulating wall case. Therefore, the surface conductivity of the MHD probe needs to be taken into account for the future flow manipulation experiments with the MHD probe.

5. Conclusion and outlook

A methodology to assess the MHD-relevant parameters in high enthalpy air plasma for flow manipulation experiments was outlined and successfully conducted for a high enthalpy air plasma condition at one of the PWT facilities of IRS. The evaluated conditions are representative for enthalpies of hyperbolic to high-elliptical re-entry trajectories into Earth's atmosphere. The derived Stuart and Hartmann numbers are indicating that the Lorentz forces will be dominant by orders of magnitude compared to the inertia and viscous forces of the plasma flow when the MHD probe will be introduced to the plasma flow. Additionally, the magnetic Reynolds number was moderately low indicating that the magnetic field won't be frozen into the flow field during flow manipulation experiments within the MEESST project. A significant MHD effect can thus be expected. Within the MEESST project, the findings provide the baseline of theoretical assessments of future flow manipulation experiments and are considered as a point of departure for future experimental studies.

In future experimental studies, other OES methods like the H_α / H_β will be employed to verify the found electron temperature and density apart from PLTE and LTE assumptions. Additionally, the investigation of the MHD flow parameters in the boundary layer of the MHD probe is of major interest of future MHD flow manipulation experiments to fundamentally investigate possible MHD effects as already been observed in similar experiments in argon plasma flows.

CRediT authorship contribution statement

Johannes W. Oswald: Writing – original draft, Visualization, Validation, Methodology, Formal analysis, Data curation, Conceptualization. **Alexander Behnke:** Writing – review & editing, Writing – original draft, Methodology, Formal analysis, Data curation. **Georg Herdrich:** Writing – review & editing, Supervision, Resources, Project administration, Funding acquisition. **Sonja I. Schlachter:** Writing – review & editing, Resources. **Matthieu Dalban-Canassy:** Writing – review & editing, Resources. **Andrea Lani:** Writing – review & editing, Project administration, Funding acquisition.

Declaration of competing interest

The authors declare that they have no known competing financial interests or personal relationships that could have appeared to influence the work reported in this paper.

Data availability

Data will be made available on request.

Acknowledgments

This project has received funding from the European Union's Horizon 2020 Research and Innovation Program under grant agreement 899298. This paper reflects only the author's view, and the European Commission is not responsible for any use that may be made of the information it contains.

References

[1] F.F. Chen, Introduction to Plasma Physics and Controlled Fusion, third ed., Springer Cham, 2016, http://dx.doi.org/10.1007/978-3-319-22309-4.

[2] A. Lani, V. Sharma, V.F. Giangaspero, S. Poedts, A. Viladegut, O. Chazot, J. Giacomelli, J. Oswald, A. Behnke, A.S. Pagan, G. Herdrich, M. Kim, N.D. Sandham, N.L. Donaldson, J. Thoemel, J.C. Duncan, J.S. Laur, S.I. Schlachter, R. Gehring, M. Dalban-Canassy, J. Tanchon, V.G. e, P. Leyland, A. Casagrande, M. La Rosa Betancourt, M. Collier-Wright, E. Bögel, A magnetohydrodynamic enhanced entry system for space transportation: MEESST, J. Space Saf. Eng. (2022) http://dx.doi.org/10.1016/j.jsse.2022.11.004.

[3] S.I. Schlachter, A. Drechser, R. Gehring, J. Willms, M. Eisele, F. Gretschmann, S. Westenfelder, F. Hornung, V. Große, A. Smara, M. Dalban-Canassy, J.W. Oswald, A. Behnke, A.S. Pagan, G. Herdrich, A. Viladegut, A. Lani, Design, fabrication and test of high temperature superconducting magnet for heat flux and radio blackout mitigation experiments in plasma wind tunnels, in: 24th Joint CEC/ICMC, Honolulu, Hawaii, 2023.

[4] E.L. Resler, W.R. Sears, The Prospects for Magneto-Aerodynamics, J. Aerosp. Sci. 25 (4) (1958) 235–245, http://dx.doi.org/10.2514/8.7604.

[5] E.L. Resler, W.R. Sears, The prospects for magneto-aerodynamics - correction and addition, J. Aerosp. Sci. 26 (5) (1959) 318, http://dx.doi.org/10.2514/8.8062.

[6] P.O. Jarvinen, On the Use of Magnetohydrodynamics During High Speed Re-Entry, Technical Report NASA CR-206, NASA, 1965.

[7] J. Giacomelli, G. Herdrich, J.W. Oswald, A.S. Pagan, A. Behnke, T.W. Hyde, R. Laufer, Experimental and numerical studies of MHD effects on plasma flows for re-entry applications, in: 72nd International Astronautical Congress, IAC, International Astronautical Federation (IAF), Dubai, United Arab Emirates, 2021.

[8] A. Knapp, H. Fulge, G. Herdrich, N. Ono, R. Wenitz, M. Auweter-Kurtz, H.-P. Roser, S. Fasoulas, Investigation of MHD Impact on Argon Plasma Flows by Variation of Magnetic Flux Density, Open Plasma Phys. J. 5 (2012) 11–22, http://dx.doi.org/10.2174/1876534301205010011.

[9] S. Kranc, M.C. Yuen, A.B. Cambel, Experimental Investigation of Magnetoaerodynamic Flow Around Blunt Bodies, Technical Report NASA CR-1393, NASA, 1969.

[10] Y. Takizawa, A. Matsuda, S. Sato, T. Abe, D. Konigorski, Experimental investigation of the electromagnetic effect on a shock layer around a blunt body in a weakly ionized flow, Phys. Fluids 18 (11) (2006) 117105, http://dx.doi.org/10.1063/1.2375076.

[11] M. Kawamura, Y. Nagata, H. Katsurayama, H. Otsu, K. Yamada, T. Abe, Magnetoaerodynamic force on a magnetized body in a partially ionized flow, J. Spacecr. Rockets 50 (2) (2013) 347–351, http://dx.doi.org/10.2514/1.A32279.

[12] A. Lefevre, D.E. Gildfind, R.J. Gollan, P.A. Jacobs, C.M. James, Magnetohydrodynamic experiments of total heat flux mitigation for superorbital earth reentry, AIAA J. 60 (9) (2022) 5046–5059, http://dx.doi.org/10.2514/1.J061771.

[13] S. Löhle, F. Zander, M. Eberhart, T. Hermann, A. Meindl, B. Massuti-Ballester, D. Leiser, F. Hufgard, A.S. Pagan, G. Herdrich, S. Fasoulas, Assessment of high enthalpy flow conditions for re-entry aerothermodynamics in the plasma wind tunnel facilities at IRS, CEAS Space J. 14 (2022) 395–406, http://dx.doi.org/10.1007/s12567-021-00396-y.

[14] P.A. Davidson, Introduction to Magnetohydrodynamics, second ed., Cambridge University Press, 2016, http://dx.doi.org/10.1017/9781316672853.

[15] M.J. Brunner, The effects of hall and ion slip on the electrical conductivity of partially ionized gases for magnetohydrodynamic re-entry vehicle application, J. Heat Transfer 84 (1962) 177–184, http://dx.doi.org/10.1115/1.3684327.

[16] A. Dinklage, T. Klinger, G. Marx, L. Schweikhard (Eds.), Plasma Physics - Confinement, Transport and Collective Effects, first ed., Springer Berlin, Heidelberg, 2005, http://dx.doi.org/10.1007/b103882.

[17] J. Meichsner, M. Schmidt, R. Schneider, H.-E. Wagner (Eds.), Nonthermal Plasma Chemistry and Physics, first ed., CRC Press, 2013, http://dx.doi.org/10.1201/b12956.

[18] L. Lamb, S.-C. Lin, Electrical conductivity of thermally ionized air produced in a shock tube, J. Appl. Phys. 28 (7) (1957) 754–759, http://dx.doi.org/10.1063/1.1722849.

[19] Y. Itikawa, Momentum-transfer cross sections for electron collisions with atoms and molecules, At. Data Nucl. Data Tables 14 (1) (1974) 1–10, http://dx.doi.org/10.1016/S0092-640X(74)80026-4.

[20] G.K. Batchelor, H.K. Moffatt, M.G. Worster (Eds.), Perspectives in Fluid Dynamics - A Collective Introduction to Current Research, Cambridge University Press, 2000, pp. 347–391.

[21] S.O. Macheret, M.N. Shneider, R.B. Miles, Magnetohydrodynamic and electrohydrodynamic control of hypersonic flows of weakly ionized plasmas, AIAA J. 42 (7) (2004) 1378–1387, http://dx.doi.org/10.2514/1.3971.

[22] G. Herdrich, M. Fertig, S. Löhle, Experimental simulation of high enthalpy planetary entries, Open Plasma Phys. J. 2 (1) (2009) 150–164, http://dx.doi.org/10.2174/1876534300902010150.

[23] J.W. Oswald, G. Herdrich, A.S. Pagan, A. Behnke, J. Giacomelli, Evaluation of high enthalpy air plasma conditions for investigation of magnetohydrodynamic flow interactions, in: 2nd International Conference on Flight Vehicles, Aerothermodynamics and Re-Entry Missions & Engineering, FAR, Heilbronn, Germany, 19–23.

[24] A.F. Kolesnikov, Extrapolation from High Enthalpy Tests to Flight Based on the Concept of Local Heat Transfer Simulation, RTO AVT course on "Measurements Techniques for High Enthalpy and Plasma Flows", Rhode-Siant-Genèse, Belgium, 1999.

[25] G. Pretzler, A new method for numerical Abel-inversion, Zeitschrift Naturforschung 46a (1991) 639–641, http://dx.doi.org/10.1515/zna-1991-0715.

[26] H. Burghaus, C.F. Kaiser, A.S. Pagan, S. Fasoulas, G. Herdrich, Aerothermodynamic characterization of an inductively generated CO_2 plasma by laser absorption spectroscopy, in: AIAA SciTech 2022 Forum, San Diego, CA, AIAA 2022-1617, 2022, http://dx.doi.org/10.2514/6.2022-1617.

[27] G.J. Tallents, An Introduction To the Atomic and Radiation Physics of Plasmas, Cambridge University Press, 2018, pp. 113–126, http://dx.doi.org/10.1017/9781108303538.007.

[28] N. Ohno, M.A. Razzak, H. Ukai, S. Takamura, Y. Uesugi, Validity of electron temperature measurement by using Boltzmann plot method in radio frequency inductive discharge in the atmospheric pressure range, Plasma Fusion Res. 1 (028) (2006) http://dx.doi.org/10.1585/pfr.1.028.

[29] B. van der Sijde, J.A.M. van der Mullen, Temperature determination in non-LTE plasmas, J. Quant. Spectrosc. Radiat. Transfer 44 (7) (1990) 39–46, http://dx.doi.org/10.1016/0022-4073(90)90079-L.

[30] M.W.G. Winter, Emissionsspektroskopische Untersuchung der Umströmung von Probenkörpern in hochenthalpen Plasmaströmungen (Ph.D. thesis), Universität Stuttgart, 2006, http://dx.doi.org/10.18419/opus-3734.

[31] T. Hermann, Emissionsspektroskopische Analyse einer hyperbolischen Wiedereintrittsströmung im Plasmawindkanal (Ph.D. thesis), Universität Stuttgart, 2017, http://dx.doi.org/10.18419/opus-9584.

[32] B.J. McBride, S. Gordon, Computer Program for Calculation of Complex Chemical Equilibrium Compositions and Applications, Technical Report NASA Reference Publication RP-1311, NASA, 1996.

[33] A. Sperber, C. Korn, O. Nimer, C.F. Kaiser, J.W. Oswald, G. Herdrich, A. Lani, M. Fertig, Numerical rebuilding of plasma wind tunnel experiments for investigation of magnetohydrodynamic flow interactions within the EU project MEESST, in: Aerospace Europe Conferece 2023, Lausanne, Switzerland, 2023.

[34] D.C. Howell, Statistical Methods for Psychology, seventh ed., Cengange Wadsworth, Belmont, CA, 2009.

[35] M. Capitelli, G. Colonna, D. Giordano, L. Maraffa, A. Casavola, P. Minelli, D. Pagano, L. Pietanza, F. Taccogna, Tables of Internal Partition Functions and Thermodynamic Properties of High-Temperature Mars-Atmosphere Species from 50K to 50000K, Technical Report ESA STR-246, ESA, 2005.

[36] G. Herdrich, M. Auweter-Kurtz, M. Fertig, A. Nawaz, D. Petkow, MHD flow control for plasma technology applications, Vacuum 80 (11) (2006) 1167–1173, http://dx.doi.org/10.1016/j.vacuum.2006.01.043.

[37] R.W. Ziemer, W.B. Bush, Magnetic field effects on bow shock stand-off distance, in: Phys. Rev. Lett., 1, (2) 1958, pp. 58–59, http://dx.doi.org/10.1103/PhysRevLett.1.58.

[38] H. Otsu, D. Konigorski, T. Abe, Influence of Hall effect on elcrodynamic heat shield system for reentry vehicles, AIAA J. 48 (10) (2010) 2177–2186, http://dx.doi.org/10.2514/1.40372.